SAND2018-8579J

Helical Instability in MagLIF Due to Axial Flux Compression by Low-Density Plasma

C. E. Seyler,[1, a)] M. R. Martin,[2, b)] and N. D. Hamlin[1, c)]

[1)] *Laboratory of Plasma Studies, Cornell University*

[2)] *Sandia National Laboratories*

The MagLIF (Magnetized Liner Inertial Fusion) experiment at Sandia National Labs is one of three main approaches to inertial confinement fusion. Radiographic measurements of the imploding liner have shown helical structuring that was not included in MagLIF scaling calculations but that could fundamentally change the viability of the approach. We present the first MagLIF linear dynamics simulations, using extended magnetohydrodynamical (XMHD) as well as standard MHD modeling, that reproduce these helical structures, thus enabling a physical understanding of their origin and development. Specifically it is found that low-density plasma from the simulated power flow surfaces can compress the axial flux in the region surrounding the liner, leading to a strong layer of axial flux on the liner. The strong axial magnetic field on the liner imposes helical magneto-Rayleigh-Taylor (MRT) perturbations into the imploding liner. A detailed comparison of XMHD and MHD modeling shows that there are defects in the MHD treatment of low-density plasma dynamics that are remedied by inclusion of the Hall term that is included in our XMHD model. In order to obtain fair agreement between XMHD and MHD great care must be taken in the implementation of the numerics, especially for MHD. Even with a careful treatment of low-density plasma, MHD exhibits significant shortcomings that emphasize the importance of using XMHD modeling in pulsed-power driven high-energy-density (HED) experiments. The present results may explain why past MHD modeling efforts have failed to produce the helical structuring without initially imposing helical perturbations.

PACS numbers: 52.30.Cv, 52.30.Ex, 52.58.Lq, 52.65.Kj
Keywords: MagLIF, extended-MHD, Hall effect, simulation, discontinuous Galerkin method

[a)]Electronic mail: ces7@cornell.edu
[b)]Electronic mail: mrmarti@sandia.gov
[c)]Electronic mail: nhamlin2002@yahoo.com

I. INTRODUCTION

The MagLIF (Magnetized Liner Inertial Fusion) experiment[1] at Sandia National Labs is one of the United States' three main approaches to inertial confinement fusion, the other two being laser-driven indirect drive fusion efforts at the National Ignition Facility in Livermore and laser-driven direct drive at the OMEGA facility in Rochester. MagLIF has achieved impressive results in a series of integrated experiments that have demonstrated the benefits of a preimposed axial magnetic field on yield and alpha confinement.[2,3] A puzzling result found in the experiment was the observation of a helical structure in the partially imploded liner that seemed to imply an axial magnetic field many times larger than predicted by the national laboratory MHD codes utilized in the design and scaling predictions of the experiments.[2–4]. The initial 10 T magnetic field applied in the experiments was not predicted by the calculations to change appreciably in the region immediately outside the liner surface where the Magneto-Rayleigh Taylor instability forms. It was expected that during the growth of this instability the azimuthal field would be tens to hundreds of times stronger than the applied axial field. Thus the expected result was that any striations created by a field-aligned instability, such as the MRT instability, would imply a pitch close to 0 degrees; however, the observed pitch was close to 20 degrees. These results implied that either the axial magnetic field was in the range of several hundred Tesla or that the helical structure was due to the seeding effect of an early time instability such as the electrothermal instability.[3]

This result was a surprise as it did not seem plausible that the axial magnetic field could be that large in the region outside the liner. Thus, the helical mode has not been included in scaling calculations for MagLIF, but could drastically impact the viability of the approach. Recent experimental and theoretical work by Yager-Elorriaga et al. have shown that an unstable helical MRT mode can be generated in thin Aluminum liners by either imposing an applied axial field, imposing helical seed perturbations, or a combination of magnetic field and helical perturbations.[5] Recent direct measurements of the inertial confinement time in fast Beryllium liner implosions point out the importance of modeling the liner dynamics correctly as it connects the shell instability to the loss of pressure and confinement time at stagnation determined through a combination of MHD simulation and experiments.[6] The body of these results motivates the need for a physi-

cal understanding of how this helical mode originates and develops in the context of the MagLIF experiment.

We present simulations that, for the first time, reproduce these helical perturbations, through the stable compression and amplification of an applied axial magnetic field onto the liner by the surrounding low-density plasma. What had not been appreciated is that the low-density plasma from the inner MITL (magnetically insulated transmission line) is capable of supporting currents that could have a significant effect on the dynamics of the implosion. Evidence of current shorting in the inner MITL suggests that this region could be a source of low-density plasma.[7] The origin of this plasma is unclear at this time, but is believed to be from either metal ablation or release of surface contaminants. A suggestion was proposed by Ryutov that this plasma may lead to magnetic flux compression onto the liner and could thus account for a strong axial field component, subsequently leading to helical MRT perturbations. This suggestion has partially motivated the present study.[8]

A comparison of the two plasma models MHD and XMHD is needed to understand why previous MHD models have failed to reproduce the helical instability. The essential difference between the models is the presence of the Hall term in the XMHD model. This effort has been complicated by several important differences between the models that have made a direct and meaningful comparison difficult. In overcoming these difficulties we have learned much about the fundamental properties of both models and a primary goal of this paper is to point out these differences so that the limitations of MHD are considered in simulations of HED experiments, and in particular the MagLIF experiment.

An important question that needs to be answered is why previous studies using MHD have not produced the helical instability in the manner proposed in this paper, namely through low-density plasma compression of axial flux onto the liner? There seem to be two distinctly different types of explanations. The first is that previous simulations did not consider the low-density plasma surrounding the liner either because it was not produced in the simulations or it was suppressed by design. If either is the case then clearly the flux compression mechanism is not applicable as there is no plasma to do the compression of the axial field. The second possible explanation is that the MHD model does not lead to sufficient flux compression even when low-density plasma surrounding the liner is present. We have found that this is a much more challenging possibility to explore for reasons that we make clear in this paper.

Before proceeding with the description of the XMHD model, we summarize the challenges we have encountered in comparing the models and the steps taken to meet these challenges. A major conclusion of this paper is that simulations using the MHD model can lead to strong axial flux compression onto the liner and produce the helical instability. However, the unphysical nature by which MHD advects low-density plasma in which the ion inertial length is significant and for which the Hall parameter is large, introduces numerical challenges that must be overcome in order to produce these results. Specifically we have found that, under MagLIF conditions and using our numerical implementation that for densities near or below 10^{23} m^{-3}, the MHD simulations exhibit a serious thermal runaway instability of a numerical nature that usually leads to simulation crashes. We were eventually successful in eliminating this instability in a manner that allows for a meaningful comparison of MHD and XMHD, but before we found a satisfactory solution we tried several other approaches that are known to be widely used in MHD simulations. These other approaches greatly reduced the flux compression efficiency to the extent that no helical instability was found. The unsatisfactory approaches used to eliminate the numerical thermal instability were: a.) to limit the current in the low-density region by application of a current limiter, b.) to introduce a so-called vacuum resistivity that effectively limits the current in the low-density plasma, and c.) use a density floor much higher than is desired. Approaches a.) and b.) tend to dissipate the flux that is compressed onto the liner to values much lower than XMHD simulations, for which none of these instability fixes are necessary. Approach c.) does not produce sufficient plasma to be effective in flux compression.

We cannot be sure that other researchers using MHD codes have encountered the same issues with MHD simulation at low densities under MagLIF conditions, as our difficulties may stem from our particular numerical approach and may not be applicable to other codes using a different method. However, we will present an argument as to how this instability can arise in MHD and how the Hall term can mitigate it, thus supporting our position that the best way to avoid the pitfalls of an MHD treatment of low-density plasma is to treat the physics correctly and include the Hall term in the Generalized Ohm's law.

The outline of the paper is a follows. In section II we introduce the XMHD model and discuss the numerical method and the relaxation method used to solve the GOL. We point out the modification of the relaxation method that eliminates the numerical

thermal runaway instability in the MHD limit. This modification was not present in the version originally proposed by Seyler and Martin[9]. In section III we discuss the important differences between the MHD and XMHD models that impact the results. In section IV we discuss the different simulations and the results. In section V we summarize our results and draw conclusions.

II. THE XMHD EQUATIONS AND NUMERICAL METHOD

We use a discontinuous Galerkin (DG) method to solve the following extended MHD equations in semi-conservative form including the Hall term and displacement current, which are not included in the usual MHD model.[9,10] The equations using standard notation are:

$$\partial_t \rho + \nabla \cdot (\rho \mathbf{u}) = 0 \tag{1}$$

$$\partial_t (\rho \mathbf{u}) + \nabla \cdot (\rho \mathbf{u}\mathbf{u}) + \nabla p = \mathbf{J} \times \mathbf{B} \tag{2}$$

$$\partial_t \mathcal{E} + \nabla \cdot [\mathbf{u}(\mathcal{E} + p)] = \mathbf{u} \cdot (\mathbf{J} \times \mathbf{B}) + \eta \mathbf{J}^2 \tag{3}$$

$$\partial_t \mathbf{B} + \nabla \times \mathbf{E} = 0 \tag{4}$$

$$\partial_t \mathbf{E} = c^2 (\nabla \times \mathbf{B} - \mu_0 \mathbf{J}) \tag{5}$$

$$\partial_t \mathbf{J} = \frac{n_e e^2}{m_e} \left(\mathbf{E} + \mathbf{u} \times \mathbf{B} - \frac{1}{n_e e} \mathbf{J} \times \mathbf{B} - \eta \mathbf{J} \right) \tag{6}$$

where the pressure is found from

$$p = (\gamma - 1) \left(\mathcal{E} - \frac{1}{2} \rho u^2 \right) \tag{7}$$

Radiation effects are not included in the present model due to these effects being of minimal importance for Beryllium tamper dynamics and that we are not studying very late-time behavior during the stagnation phase when the temperature rises suddenly and when radiation and thermal conduction are important.

The equations are non-dimensionalized using characteristic length L_0, time t_0, ion density n_0 and mass m_i scales. Assuming that the speed is normalized relative to the characteristic Alfvén speed taken to be $v_0 = L_0/t_0 = B_0/\sqrt{m_i n_0 \mu_0}$, and the characteristic magnetic field is $B_0 = \sqrt{m_i n_0 \mu_0}\, v_0$, then all field variables are non-dimensionalized as follows:

$\tilde{\rho} = \rho/m_i n_0$, $\tilde{u} = u/v_0$, $\tilde{\mathcal{E}} = \tilde{E}/m_i n_0 v_0^2$, $\tilde{B} = B/B_0$, $\tilde{E} = E/v_0 B_0$, and $\tilde{J} = J\mu_0 L_0/B_0$. The dimensionless dynamic Hall parameter $\delta_i \equiv \sqrt{m_i/n_0 e^2 \mu_i}/L_0$, which is the ratio of the Hall term to the MHD inductive term, appears as a scale-dependent parameter multiplying the Hall term in Eq. (6). The resistive Hall parameter Ω_e/ν_{ei}, which is the ratio of the Hall term to the Ohmic term, does not appear in the equations directly. The GOL has the dimensionless parameter $1/\epsilon \equiv L_0^2/(m_e/n_0 e^2 \mu_0)$ as a coefficient of the term in square brackets and the Ampere-Maxwell equation (5) has a dimensionless coefficient $1/\delta \equiv v_0^2/c^2$ as the coefficient replacing c^2. Upon non-dimensionalization the tildes are dropped.

The generalized Ohm's law, the Ampere-Maxwell equation, and the momentum equation are solved by a semi-implicit relaxation method that was described in Seyler and Martin[9] for the GOL and Ampere-Maxwell equations. Here we present an improved method that includes the momentum equation. Including the momentum equation in the semi-implict advance yields improved stability with respect to thermal runaway. We comment more on this issue later.

The relaxation method begins with an explicit partial advance of the flux terms containing the spatial derivatives. The partially advanced quantities are denoted with superscript *.

$$\rho^* = \rho^n - \Delta t \, \nabla \cdot (\rho \mathbf{u})^n \tag{8}$$

$$(\rho \mathbf{u})^* = (\rho \mathbf{u})^n - \Delta t \, \nabla \cdot (\rho \mathbf{u}\mathbf{u} + \mathbf{I}p)^n \tag{9}$$

$$\mathbf{B}^* = \mathbf{B}^n - \Delta t \, \nabla \times \mathbf{E}^n \tag{10}$$

$$\mathbf{E}^* = \mathbf{E}^n + \frac{\Delta t}{\delta} \nabla \times \mathbf{B}^n \tag{11}$$

$$\mathbf{J}^* = \mathbf{J}^n \tag{12}$$

The source terms are then considered in the semi-implicit update to complete the time advance.

$$(\rho \mathbf{u})^{n+1} = (\rho \mathbf{u})^* + \Delta t \, \mathbf{J}^{n+1} \times \mathbf{B}^* \tag{13}$$

$$\mathbf{E}^{n+1} = \mathbf{E}^* - \frac{\Delta t}{\delta} \mathbf{J}^{n+1} \tag{14}$$

$$\mathbf{J}^{n+1} = \mathbf{J}^* + \frac{\Delta t}{\epsilon} \left[\mathbf{E}^{n+1} + \mathbf{u}^{n+1} \times \mathbf{B}^* - \frac{\delta_i}{n^* Z} \mathbf{J}^{n+1} \times \mathbf{B}^* - \eta^* \mathbf{J}^{n+1} \right] \tag{15}$$

We use the small parameters ϵ and δ to control the relaxation. In the present problem the electron inertia does not play a significant role, accordingly we take the relaxation parameter ϵ to be a constant at a sufficiently large value to maintain accurate relaxation conditions. For this parameter only, we fix the electron density to $n_e = 10^{-3} n_0$, where n_0 is the reference density and is equal to the solid density of Beryllium. This gives an effective electron inertial length of about 0.5 μm. In the Hall term the electron density is variable and includes ionization dynamics determined by the simple hydrogenic ionization model used in McBride and Slutz. Quasineutrality is assumed to obtain the electron density from the ion density, which is determined by the continuity equation.[11] Since the electron inertial length is under-resolved, we do not include the advection terms for the current density; hence Eq. (15) is an ordinary differential equation for the current density. The results are determined to be insensitive to the value of ϵ as long as the effective electron inertial length is under-resolved.

The relaxation method is local in space, meaning that no large linear systems of equations need to be solved since the source terms have no space derivatives. In practice, Eqs. (14) and (15) are solved analytically for $\mathbf{E}^{n+1}$ and $\mathbf{J}^{n+1}$ and the solution coded directly rather than using a numerical 6×6 matrix inversion. To see how the relaxation method works, it is revealing to take the limit of large $\Delta t/\delta$ and $\Delta t/\epsilon$ for Eqs. (14) and (15). When solved and taking the limit, the leading order terms in $\Delta t/\delta$ and $\Delta t/\epsilon$ cancel out and we have

$$\mathbf{J}^{n+1} = \nabla \times \mathbf{B}^* \tag{16}$$

$$\mathbf{E}^{n+1} = -\mathbf{u}^* \times \mathbf{B}^* + \frac{\delta_i}{n^* Z} \mathbf{J}^* \times \mathbf{B}^* + \eta^* \mathbf{J}^* \tag{17}$$

This shows that Eqs. (14) and (15) relax to Ampere's law and the Hall-MHD Ohm's law, Eqs. (16) and (17). The error terms for this method are of of order $\epsilon/\Delta t$ and $\delta/\Delta t$. Our somewhat complicated analysis shows that the errors are small for the parameters used in the simulations. This algorithm exhibits good stability properties if the time step is chosen to satisfy the CFL condition with respect to the numerical speed of light, which is typically taken to be considerably less than the physical speed of light. If instead of taking the limit of large $\Delta t/\delta$ and $\Delta t/\epsilon$, we take the limit of these parameters to be small, we would have an implicit backward Euler time advance method. In this case the

electron inertial terms are resolved and contribute to the dynamics; however, this is not the limit we are considering in this paper, as the electron inertial length is unresolved for the floor densities considered. The interested reader may wish to refer to the more detailed discussion of the relaxation method in Seyler and Martin[9] and references therein.

The equation of state (EOS) relating the internal plus kinetic energy $\mathcal{E}$ to the plasma pressure p is a Birch-Murnaghan EOS for a density greater than solid and an ideal EOS with adiabatic index of 1.25 for the lower density component.[11] A simple hydrogenic ionization model is used to compute the charge state Z for the resistivity model that approximates the metallic resistivity of Beryllium for near-solid densities and transitions to the Spitzer resistivity at lower densities.

The hydrodynamic fluxes are calculated using an HLLC solver.[12,13] It is for this reason that we use the $\mathbf{J} \times \mathbf{B}$ in the momentum equation instead of the Maxwell stress tensor, as the hydrodynamic HLLC solver is not compatible with the Maxwell stress tensor in the momentum flux. We have compared the formulations using $\mathbf{J} \times \mathbf{B}$ and the Maxwell stress flux using the local Lax-Friedrichs flux[12] and find the results are very close. The current density does not need a flux solver, since for the relaxation method the current does not need flux terms.

The simulation time is reduced by decreasing the speed of light by a factor of 30, a common technique when simulating fast z-pinches in codes that are subject to time steps restricted by the speed of light.[7] It has been determined that this reduction factor does not significantly affect the results compared to higher values of c, since $c = 10^7$ m-s^{-1} is generally much faster than the flow speed. The Alfvén and fast wave speeds are automatically limited to the numerical c due to the inclusion of displacement current and by implementing the force explicitly as $\mathbf{J} \times \mathbf{B}$ as opposed to incorporating the force into the Maxwell stress tensor and then including the electromagnetic momentum flux in the momentum equation.[14] In all simulations (except where explicitly stated) the density floor for ions is 1.2×10^{21}m^{-3}. This floor is near the lowest at which we can reliably solve the MHD model; however, we have found that XMHD can handle a floor about an order of magnitude lower or somewhat less and still produce good results.

III. THE IMPACT OF THE HALL TERM

In this section we discuss some important aspects of XMHD that will account for the differences found between XMHD and MHD. Specifically we show that the Hall term allows for a physical transition to the vacuum, that it can generate force-free currents in a manner that differs distinctly from MHD, and finally we show that the unphysical conductivity at low density for MHD can lead to a thermal runaway unless steps are taken to mitigate the numerical instability.

A. Low-density conductivity

The Hall term plays an essential role for magnetized plasma in the transition of the conductivity to a physical vacuum value at a number density of 10^{17} m^{-3}, which is typical for the 10^{-5} Torr vacuum pressure of most experiments on the Z facility. Consider the simplified case of a constant magnetic field in the z direction. The anisotropic conductivity, which includes the Hall effect, consists of three independent components, $\sigma_\parallel$, σ_P, and σ_H, which are the parallel, Pederson, and Hall components respectively. They are

$$\sigma_\parallel = \frac{1}{\eta} = \frac{ne^2}{m_e \nu_{ei}} \tag{18}$$

$$\sigma_P = \frac{ne^2}{m_e} \frac{\nu_{ei}}{\nu_{ei}^2 + \Omega_e^2} \tag{19}$$

$$\sigma_H = \frac{ne^2}{m_e} \frac{\Omega_e}{\nu_{ei}^2 + \Omega_e^2} \tag{20}$$

These components are defined as follows: The parallel conductivity refers to generation of current by the component of the E-field parallel to the B-field, the Pederson conductivity refers to the component of the E-field perpendicular to the B-field, and the Hall conductivity refers to the component in the $\mathbf{E} \times \mathbf{B}$ direction.

We seek the low-density limit in which the electron-ion collision frequency is approximately proportional to the plasma density. Thus in the limit $n \to 0 : \sigma_\parallel = 1/\eta$, $\sigma_P = 0$, and $\sigma_H = ne/B$. For MHD the conductivity is isotropic and there is only the parallel component that is the inverse of the Spitzer resistivity η. If we consider the component of the current along the electric field, which we take to be in the x direction, then the Pederson component is relevant and the above results show that the Hall term is necessary to give

zero conductivity in the direction of the electric field. Without the Hall term the conductivity is simply the inverse of the Spitzer resistivity. This is the essential reason why so many MHD codes need to use a vacuum resistivity in which the resistivity is artificially taken to be large in order to suppress currents in low-density plasma. The Hall term does this in a natural way. This result has been known for a long time[15], but in our opinion the impact of this fact has been under-appreciated. The consequences of using a vacuum resistivity in the problem considered in this paper can be profound in a negative way, that is, it can suppress physical processes.

B. Generation of force-free currents

The anisotropic conductivity due the Hall term allows for a mechanism through which force-free currents can be directly produced by a driving electric field. We assume that the axial electric field E_z is the primary current driver, the magnetic field in cylindrical coordinates is $\mathbf{B} = \hat{\theta}B_\theta + \hat{z}B_z$, the resistive Hall parameter is large ($\Omega_e \gg \nu_{ei}$), and there are no flows. Then from the conductivity tensor components given in Eqs. (18) - (20) it follows that $\sigma_\parallel/\sigma_H \gg 1$ and that the current follows the field lines. Thus the current driven by the axial electric field is approximately

$$\mathbf{J} = \mathbf{B}\,\frac{B_z E_z}{B^2\eta}\,, \tag{21}$$

which is identically force-free. Thus the Hall conductivity facilitates an azimuthal current generating the axial magnetic field that is driven by the axial electric field. The equivalent result for MHD is $J_\theta = 0$ and $J_z = E_z/\eta$. Consequently, XMHD can generate an additional azimuthal current that can potentially amplify the applied axial field over and above that due to flux compression, for which the azimuthal current is given by $J_\theta = u_r B_z/\eta$. We believe that this effect accounts for the substantial differences between XMHD and MHD with respect to the generation and distribution of the force-free currents in low-density regions.

This result only holds within an ion inertial length ($\delta_i = c/\omega_{pi}$) of the plasma-vacuum boundary since the converging radial flow times the azimuthal magnetic field ($-u_r B_\theta$) generates an axial electric field that partially cancels the driving electric field. Within this layer, the magnetic field decouples from the mass flow, allowing the driving electric field

field to penetrate a distance δ_i into the plasma, thereby driving the approximate force-free current given by Eq. (21).

For the simulations that we consider in this paper, the boundary conditions (periodic or conducting) do not allow for additional net axial flux crossing the plane from the liner to the conducting wall to enter the system. However, under conditions in which magnetic flux can be introduced through the boundaries, the force-free mechanism due to anisotropic conductivity can play an important role and can allow for the generation of additional flux beyond that produced by the ideal magnetic flux advection of the ideal Ohm's law. This mechanism, which we believe is related to recent work due to Velikovich (personal communication), will be considered in a future paper.

C. Ohmic heating

The numerical thermal runaway instability arises due to the large conductivity at low densities implicit in the resistive MHD Ohm's law without a vacuum resistivity. To see how this can happen and how using an implicit update to the momentum equation can inhibit this instability, consider the Ohmic heating rate due to the electric field. The electric field produced by the MagLIF pulse can reach the order of 10^9 Vm^{-1} in the load region. Consider a simple version of the energy equation $\dot{\mathcal{E}} = \mathbf{J} \cdot \mathbf{E}$ where $\mathcal{E}$ has both mechanical and thermal energies.

In the plasma, estimates of the current and density give a rate of change of energy of the order of 10^{18} Wm^{-3}. Using $E \sim 10^9$ Vm^{-1} for the vacuum inductive electric field and $J \sim 10^{12}$ Am^{-2} for the current density in the low-density plasma, this gives a change in energy per particle over one time step ($\Delta t = 6{\times}10^{-13}$) of about 10^5 eV. Clearly this does not happen in the simulations of this model. The reason is that we did not consider the term $\mathbf{u} \times \mathbf{B}$ in our estimate for the electric field in the plasma. However, at the plasma-vacuum interface the electric field will be very high and the plasma will respond by developing a flow to reduce it. The numerical issue arises because with the explicit Heun Runge-Kutta time advance of the fluid velocity the flow lags the calculation of the electric field and therefore the frame-dependent electric field can be too large, leading to too much heating and thermal runaway. If the momentum equation is updated after the current and electric field semi-implicit advance then this issue does not arise.

Another way to deal with this issue is to reduce the time step; however we have found that this requires a time step that is prohibitively small. The best method is to use the semi-implicit update of the momentum equation given in Eq. (13). We have found that this method is sufficient to prevent thermal runaway for MHD. For XMHD it is not necessary to use the implicit update of the momentum as the low-density cross-field currents are naturally suppressed by the Hall term. For the sake of a fair comparison, we use the same time advance method for both MHD and XMHD that has the semi-implicit momentum update.

As discussed in Sec. III A a vacuum resistivity can be used to suppress low-density currents and this can stabilize the thermal runaway. An alternative method to reduce the current in the low-density plasma is to simply limit the current to a sufficiently low value as to prevent thermal runaway. Since the current density is an independent variable, this is straightforward to do in our code. The codes that compute the current density through Ampere's law do not have this option, since $\mathbf{J} = \nabla \times \mathbf{B}/\mu_0$. While we have found that current limiting can indeed stabilize thermal runaway, it suffers from the same issue as the vacuum resistivity in that it dissipates magnetic flux and thereby reduces flux compression of the axial field, yielding results with much lower compressed axial flux than XMHD.

Another way to eliminate the thermal runaway problem is to use a higher density floor. We have found that a floor of 10^{-6} of solid Be density is sufficient for this purpose if no other form of current limiting is used, but the problem is that this corresponds to a density around 10^{23} m^{-3}, which is likely too high to accurately represent the ablation plasma in the experiment. For this reason we have decided that the density floor of 10^{-8} times solid density is probably adequate,which in any case is the lowest floor we can use for MHD. Using this floor, MHD requires either a vacuum resistivity, a current limiter, or an implicit update of the momentum to prevent thermal runaway. For the purposes of comparing MHD and XMHD we believe the implicit update of the momentum is the best approach and is the one used in all results presented except for figure 12. We point out that XMHD does not require any of these means to stabilize thermal runaway as it has never been an issue for the density floor we use in all results displayed.

D. Treatment of the plasma-vacuum interface

The existence of a plasma-vacuum interface poses significant challenges for a fluid code. Our code PERSEUS utilizes a density floor, which is the only way we have found to formulate the numerical problem. We are able to run the code for densities as low as 10^{-9} of solid density Be if we use XMHD. For MHD we need a floor of about an order of magnitude higher. An issue that would seem to confront all codes that use a floor is how to treat cells that have a density within a small fraction of the floor value. We have found it necessary to define a buffer region that is a small fraction above the floor. In the simulations presented here this buffer region is between the floor and 1.001 times the floor for the 2D simulations and 1.01 times the floor for 3D simulations. If the density falls into this buffer region the current is set to zero; however, the density is not reset as this would violate mass, momentum, and energy conservation. Before this reset is performed the DG method uses a positivity preserving limiter to prevent the density and pressure from becoming negative and falling below the floor values. This limiter conserves mass, momentum, and energy. This method was discussed in Zhao et al. and references therein.[10] This procedure works well for the XMHD case, but for MHD there arises another issue that is handled in a different manner.

We have found that, despite our attention to the details of the treatment of low-density plasma, MHD can exhibit anomalously fast (near the numerical speed of light) diffusion of the very hot plasma within the density buffer region. This anomalous diffusion does not happen in XMHD, presumably due to the more correct treatment of the low-density plasma. To mitigate this unphysical behavior in MHD, in addition to the positivity preserving limiter, we use a type of interface tracker in the HLLC flux computation, which works as follows. Before the HLLC fluid flux is computed through a cell interface, we test whether the density on either side of that interface falls below the upper limit of the density buffer region. If, for example, this occurs on the left side of an interface, then we reset the fluid on the left side to vacuum values, i.e. the vacuum limit of the HLLC computation, corresponding to zero density, momentum, energy, pressure, and velocity. Note that because this reset only applies within the HLLC fluid flux computation, the density and pressure are not reset to floor values. We also reset the fast wave speed to its vacuum value, which in the presence of magnetic field is the numerical speed of light,

and is otherwise zero. If both sides of the interface fall below the density buffer limit, then we simply zero out the fluid flux through that interface. This interface tracker mitigates the unphysical diffusion for MHD and has a minimal effect on XMHD computations.

IV. SIMULATION RESULTS

We present and discuss several types of simulations. First we perform 2D axisymmetric ($r - z$) simulations in which we initialize a feed section to guide the TEM wave into the region above the cathode containing the liner. These 2D simulations can be done at much higher resolution than the 3D simulations, allowing us to study a larger range of parameters and validate our methods for improving stability. To control the amount of plasma originating from the feed, we inhibit the motion of the feed walls and initialize a one-cell layer of low-density plasma at 2×10^{23} m^{-3} that can evolve dynamically.

Shown in figure 1 is a cross section of the feed, cathode, liner and return current walls. This is only an approximation of the MagLIF feed geometry. The various sections are labeled accordingly. Altogether we present four simulations using this geometry. These simulations correspond to one each of MHD and XMHD with and without a plasma layer on the feed walls. The liner surface, top of the cathode, and the conducting walls above the feed slot evolve dynamically and are allowed to ablate plasma. Control of this ablation is a challenging problem in itself and a full discussion would involve more space than we could afford, although we acknowledge its importance to the problem. It is for this reason that we chose to partially control the amount of plasma entering the region surrounding the liner through the initialization of the layer on the feed walls. Controlling the amount of ablation from dynamically evolving surfaces without affecting the dynamics of the low-density plasma in an undesirable manner has proven to be a difficult problem with which we have had limited success.

The next simulations we present are 3D Cartesian in which we only consider part of the liner and initialize a region of low-density plasma surrounding the liner out to the inner radius of the feed. We impose periodic boundary conditions in the axial dimension and drive the azimuthal field from the outer x and y boundaries of the simulation domain. We present two simulations corresponding to MHD and XMHD. The purposes of these simulations are threefold. The first is that three dimensions are needed to allow

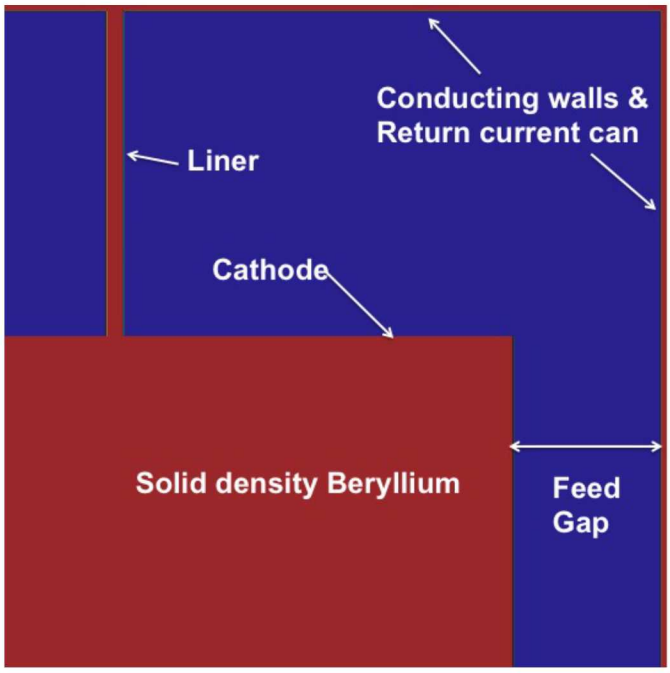

Figure 1. Shown is a diagram of the initial MagLIF conductors. The dimensions of the regions are described in the text. The power input is an azimuthal magnetic field applied at the bottom face of the bottom cell in the feed gap. The solid density Beryllium is initialized at a temperature of 0.026 eV.

for helically unstable modes. For the two-dimensional simulations we find that there is very little evidence of the MRT, presumably due to the large stabilizing axial magnetic field on the liner surface driving the pitch of the instability out of the dimensions of the simulation[5]; hence 3D simulations are required to observe the MRT. In the absence of an applied field the MRT is very robust in the 2D simulations. The second is to remove the concerns regarding the ablation of plasma from the free surfaces by explicitly preparing the low-density plasma surrounding the liner. And thirdly, to present a direct comparison between XMHD and MHD without the complications of the differing ablation rates of the two models.

The third simulation, for which we show only one case, is for a 3D XMHD simulation, which has both the feed and liner sections and has the same dimensions as the 2D axisymmetric simulations. In this case we allow all surfaces to dynamically ablate plasma and do not initialize the low-density plasma layer as was done in the 2D simulations. This simulation involves a substantial amount of computer time and was done on the

computer facilities at SNL using 4096 cores requiring 36 wall clock hours. All other simulations were performed on a workstation using 32 cores.

A. Two-dimensional r-z simulations

In figure 2 are plots at 20 ns of a 2D axisymmetric simulation including the feed section without any initial plasma layer. The liner was seeded with random 0.5% density perturbations. The bilinear DG basis is used for this simulation with a cell size of 37.5 μm. The Gaussian quadrature uses 4 internal and 2 edge points per cell. The simulation box dimensions are 15×15 mm. The liner height is 7.5 mm, the thickness is 0.385 mm, and the feed gap is 3.35 mm. The simulations are initialized with a 10 T axial (z-component) magnetic field and the azimuthal field is driven to 20 MA in 100 ns by applying the field in the gap region at the bottom using a standard $\sin^2(\pi t/2\tau)$ waveform, where τ is the 100 ns rise time. Figure 2 upper right-hand panel shows the low-density plasma originating primarily from the top of the cathode and the top wall and flowing towards the liner. Even at this early time there is significant compression of axial flux near the liner. The upper right panel displays $J_{\|}$ representing the force-free current. Comparison with the magnitude of $J_{\perp}$ presented in figure 3, shows that $J_{\|}$ is more than an order of magnitude larger than $J_{\perp}$. Thus the current in the low-density plasma is predominantly force-free in this case.

Figure 4 shows the same simulation as figure 2 at 90 ns. At this late time the compressed axial flux is in a thin layer on the surface of the liner and has reached a strength near 1000 T, which is comparable to the azimuthal field strength of around 1500 T. Note that the low-density plasma has moved into the feed region although none was initiated in the feed and the ablation was suppressed in the feed region. Examining an animated sequence of log density plots shows that this plasma flows along the cathode away from the liner and down the cathode side of the feed and eventually into the feed gap. This behavior does not occur in the MHD simulation. We believe this phenomenon is due to a Hall effect first pointed out by Kingsep et al.[16] in which magnetic flux is transported by the Hall velocity. In this case the azimuthal flux would be transported away from the liner on the cathode surface given the sign of the axial density gradient at the cathode. If the density is frozen into this flux then it would also be transported away from the liner

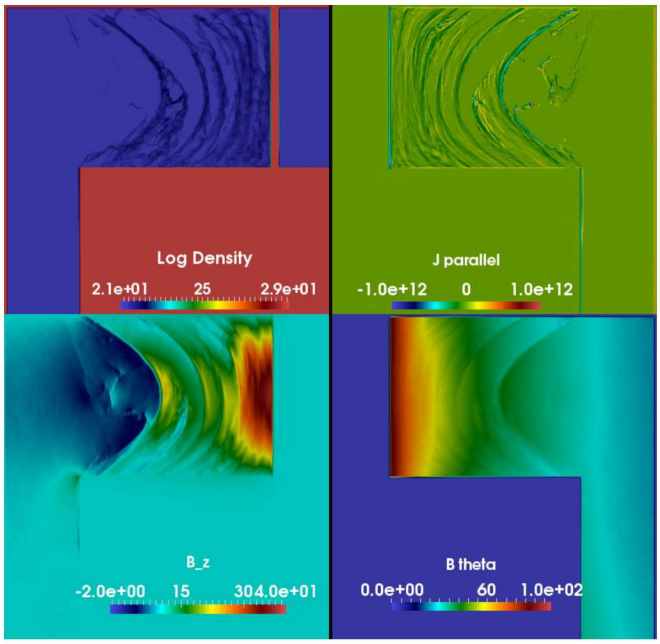

Figure 2. Two-dimensional axisymmetric XMHD simulation. The plots are log density in m^{-3}, $\mathbf{J} \cdot \mathbf{B}$, axial and azimuthal magnetic fields (in T) at 20 ns for the case in which no plasma layer is initialized on the feed walls. The low-density plasma originates primarily from the top of the cathode and carries predominantly force-free currents generating the enhanced axial magnetic field.

along the cathode surface and then down into the feed gap. Further work is needed to verify the nature of this effect.

Figure 5 shows the MHD case for the same conditions and time 20 ns as figure 2. Note that the low density plasma is not as structured and is more diffuse than the XMHD case. Also the axial magnetic field, while of comparable strength, has a different form from the XMHD case. The low-density plasma is also force-free, as it must be in order to remain where it is, but has a different structure from the XMHD case. The force-free currents for MHD are considerably weaker than XMHD, which is consistent with the force-free current generation mechanism given in Eq. (21).

Figure 6 is the MHD simulation at 90 ns to compare with the XMHD case in figure 4. At this late time the axial flux has compressed on the liner into a thin layer and is close in magnitude and structure to the XMHD case. The main differences in the late time MHD results compared to the XMHD results are in the low density and current distributions,

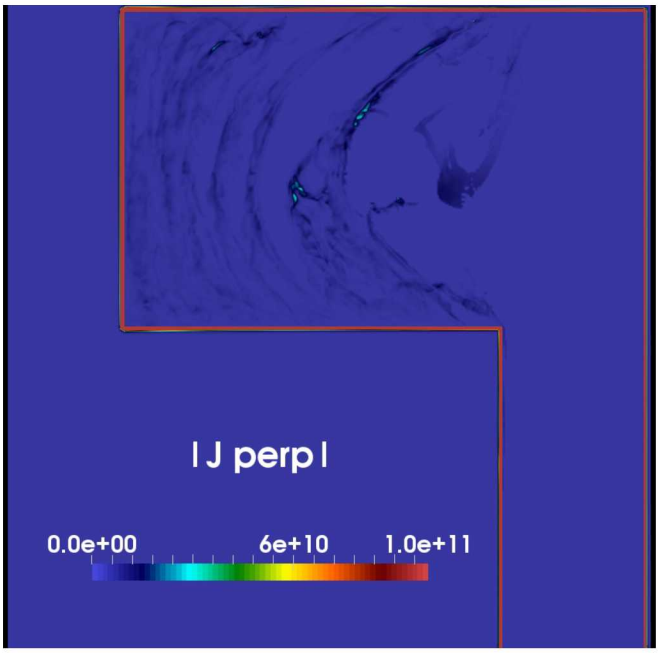

Figure 3. Two-dimensional axisymmetric XMHD simulation. This plot shows the current perpendicular to the magnetic field to compare with the parallel current shown in figure 2. Note that the perpendicular current is about an order of magnitude smaller than the parallel current.

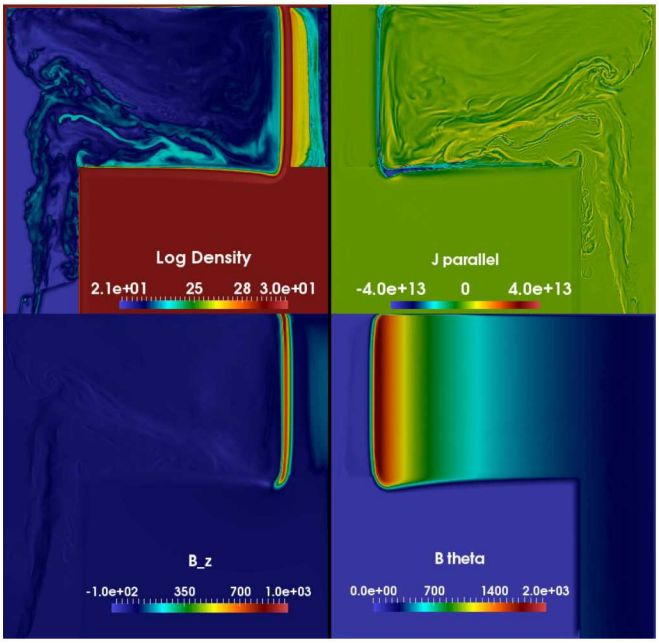

Figure 4. Same simulation as figure 2 at 90 ns. Note the much stronger axial field at this late time

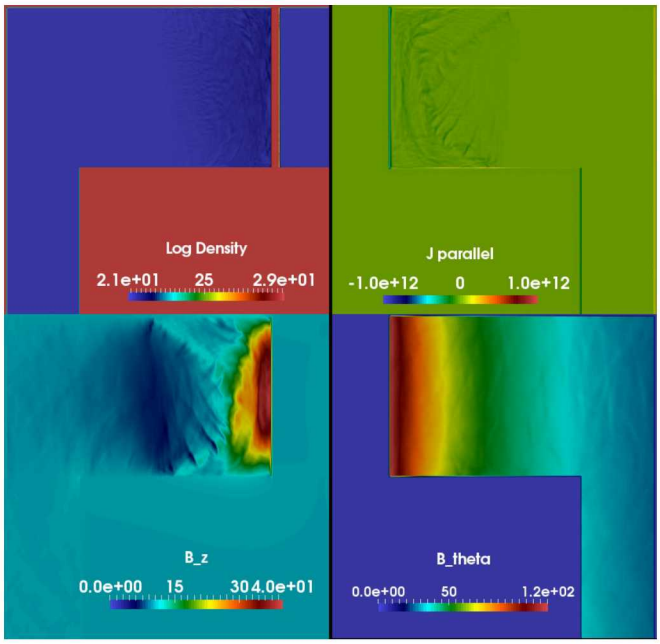

Figure 5. Same simulation parameters as figure 2 for the MHD case. Note that the axial field is approximately the same as XMHD, but has a notably different structure. Also note that the force-free current density $J_{||}$ is considerably larger in the XMHD case, which is consistent with the additional force-free current generation mechanism for Hall MHD given by Eq. (21).

whereas the magnetic field structure is very close. Note in particular that there is no low-density plasma in the feed for MHD at late times. We attribute this difference to differences in the advection of low-density plasma with and without the Hall term resulting from the Hall electric field. At this later time MHD still does not have as much force-free current as does the XMHD case at 90 ns.

Next we examine the effect of initializing a plasma layer of one cell (37.5 μm) of $2 \times 10^{23}\mathrm{m}^{-3}$ plasma on both walls in the feed gap. The XMHD simulation in figure 7 shows the initial compression of the axial field at 20 ns. Note that no current has reached the liner as it has in figure 2 due to the shorting between the anode and cathode resulting from the initial plasma layer that has blown into region above the feed gap.

Figure 8 displays the results at 40 ns, which show considerably more flux compression than the no-layer case at the same time (result not shown at 40 ns). The MHD case with a plasma layer is shown in figure 9 and has the same initialization as figure 7. The main difference is that the axial field is weaker, but wider, having approximately the same flux

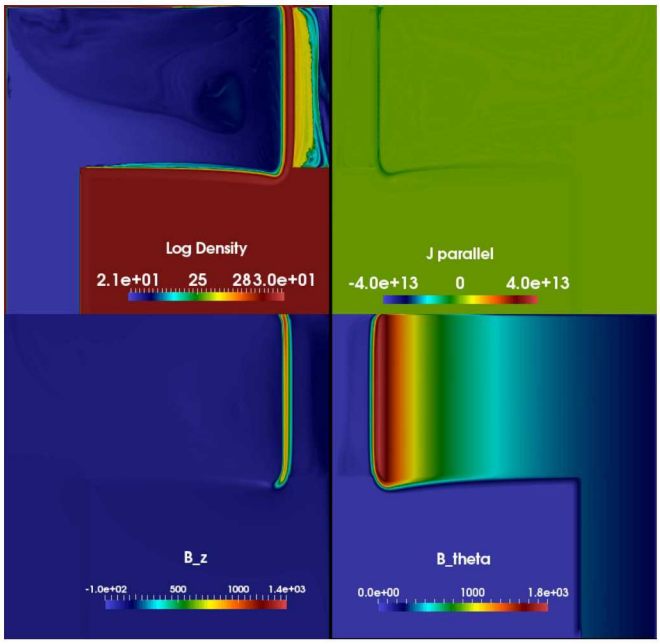

Figure 6. Same simulation parameters as figure 4 for the MHD case at 90 ns. Note that the axial field is larger than XMHD at 90 ns.

compared to XMHD. The force-free currents are somewhat smaller than XMHD for this case, but not as small when compared to the case without an initial layer shown in figures 5 and 6. At late times greater than about 80 ns the results for the magnetic field are very close, but differences remain in the current and density distribution.

Figure 10 shows the effect of a high density floor on ablation and axial flux compression in the MHD case. The floor is 2×10^{-6} of solid density or about 2.4×10^{23} m^{-3}. The left panels are the log density and axial field at 108 ns for the case in which a one-cell layer of 10^{24}m^{-3} plasma was initialized on the feed walls and the right panels are without an initial layer. This case is presented as a point of comparison to previous MHD simulations using lab codes in which the floor used is close to the value used in this case. There are several important points to make in comparing the results in figure 10 to those in figures 6 and 9. For the left panels with an initial plasma layer, the implosion radius in figure 10 at 108 ns is not as small as that in figure 6 without an initial layer at 90 ns. This is because the higher density plasma in the feed significantly delays the arrival of the current to the liner by shorting across the feed gap and the additional mass that must be moved in order for the current to reach the liner. For late times (not shown) under the

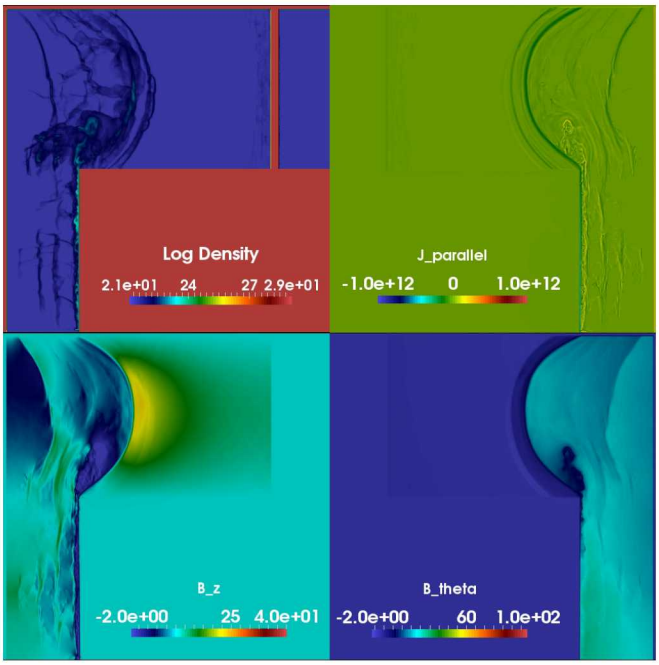

Figure 7. XMHD simulation with an initial one-cell thick plasma layer of density $2 \times 10^{23} \mathrm{m}^{-3}$ on the walls of the feed section at 20 ns. The parameters are the same as figure 2 except for the plasma layer. This plot shows the initial compression of the axial field. Note that no current has reached the liner as it has in figure 2 due to the shorting between the anode and cathode resulting from the initial plasma layer that has blown into the region above the feed gap.

conditions of figure 9, the liner implosion radius is significantly smaller, indicating that the lower density layer at 2×10^{23} m^{-3} does not inhibit the implosion as significantly as the higher layer density for the left panels of figure 10. The feed gap current shorting for the XMHD case (not shown) is also significant as is the delay in the implosion time. The results of the XMHD case are close to that of MHD. Note that the MRT instability is completely suppressed in this case due to the axisymmetric symmetry imposing the stabilizing effect of line bending of the strong axial field for axisymmetric perturbations. We would, however, expect a helical MRT instability in a three-dimensional simulation as we will show later.

The right panels, without an initial feed plasma, show no ablation from the outer surfaces of the liner, the top wall, or the top of the cathode. The lack of ablation is directly attributable to the higher density floor. In contrast, as shown in figure 6 at 90 ns, there

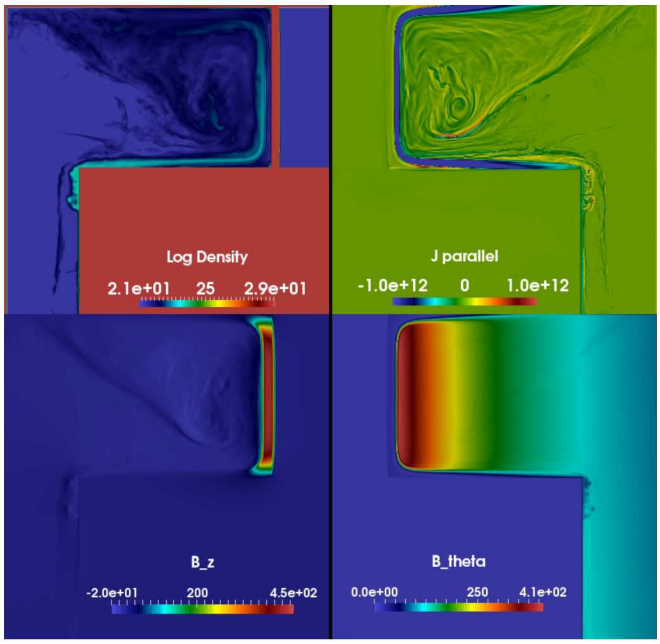

Figure 8. XMHD simulation with an initial one-cell thick plasma layer of density $2 \times 10^{23} \mathrm{m}^{-3}$ on the walls of the feed section at 40 ns. The parameters are the same as figure 7. At 40 ns the axial field has compressed onto the liner surface and has reached several hundred Tesla.

is considerable plasma surrounding the liner as well as strongly compressed field on the liner surface. Thus, there is a much smaller axial field on the liner surface and consequently there is a lack of stabilizing influence from the magnetic shear. This results in the strong MRT instability that has fed through deeply into the liner as seen in the top-right panel.[5]

B. Three-dimensional flux compression and helical MRT instability

To provide an unambiguous comparison of XMHD and MHD with respect to axial flux compression, we performed simulations of the liner surrounded by a fixed amount of low-density plasma at 10^{23} m^{-3} extending out to 20 mm, which is the same as the distance to the edge of the cathode in the 2D simulations. The initial axial field is 10 T, the boundary conditions are periodic in the axial direction, and the azimuthal field is driven at the outer walls. The simulations have a 104 μm resolution per cell using a trilinear DG basis and an 8-point Gaussian quadrature for the internal cell points and 4-point

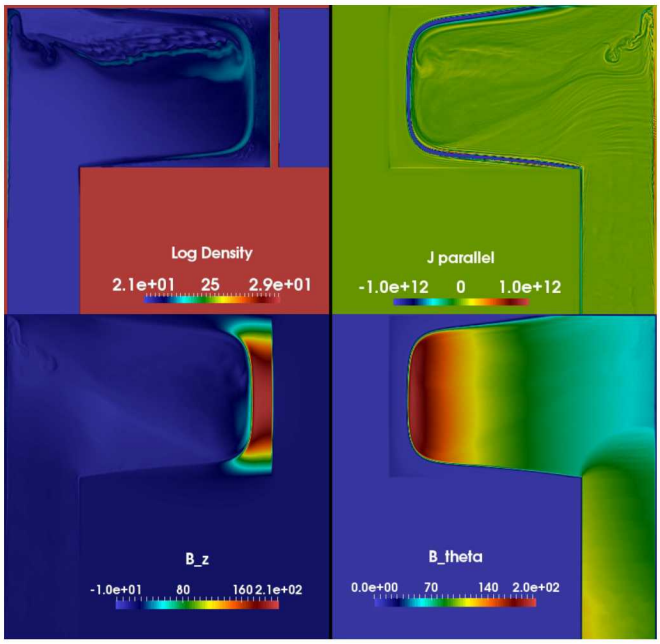

Figure 9. The MHD simulation at 40 ns to compare with the XMHD simulation in figure 8. Note the smaller axial field, but wider layer on the liner as well as the reduced force-free current in the low-density plasma region. The XMHD and MHD results for the magnetic fields at late times are very similar and thus are not shown. The currents and low-density plasma distributions are, however, significantly different in a manner similar to that at 40 ns.

Gaussian quadrature on the six faces. The liner density was seeded with 1% random perturbations in each cell.

The XMHD simulation is shown in figure 11 with the panels top to bottom showing the log density through the center, the axial magnetic field at the same scale, and the isosurface of 1.6×10^{29} m^{-3} with the magnetic field lines close to the liner surface and the color corresponding to the axial field strength. This result shows a helical MRT instability following the pitch of the magnetic field lines close to the liner surface. The resolution is is too coarse to resolve the electrothermal instability.

In figure 12 we show the density isosurface at 4×10^{29}m^{-3} at 119 ns for the same simulation as figure 11. In the left panel the color scale corresponds to the axial field strength. The middle and right panels are cut at the $x = 0$ plane with x directed into the plane. Note that the axial field intensity on the inside surface is considerably larger than outside and has a helical form. The right panel shows the density through the $x = 0$ cross-section. The

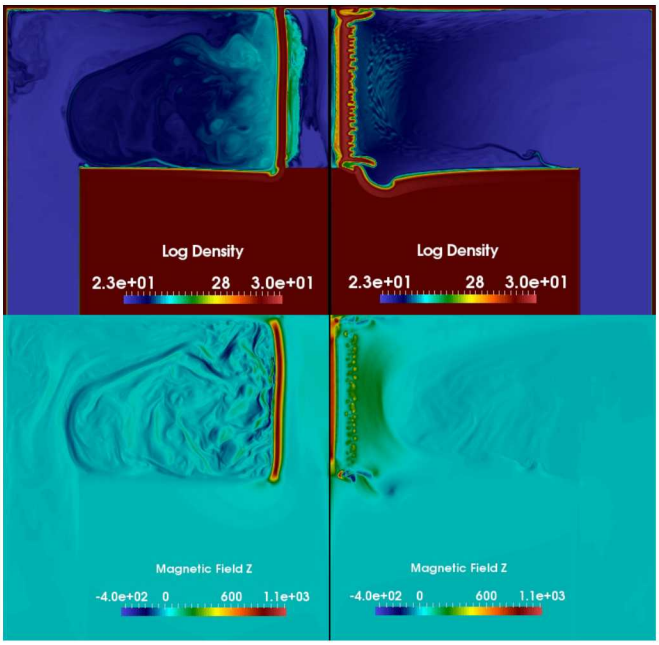

Figure 10. A comparison of the effect of a high floor density on axial flux compression for MHD. Both simulations are MHD at 108 ns. The floor density is $2.4 \times 10^{23}\mathrm{m}^{-3}$. The left panels are for a one-cell initial layer density of $10^{24}\mathrm{m}^{-3}$ on the feed walls and the right panels are without an initial layer. For reference, the centerline ($r = 0$) between the two simulations is the left boundary of the magnetic field in the lower right panel where the axial field is strongest.

theta variation of the field on the outer surface has an azimuthal mode number $m = 1$ and varies by a factor of two on the surface. This B_z variation drives an $m = 1$ kink distortion of the liner that is evident in the B_z field on the inner surface. We believe the kink distortion is more likely due to the usual MHD kink instability than to the MRT instability. This internal distortion appears to be related to the self-emission image near stagnation shown in figure 5 of Gomez et al..[17]

The corresponding MHD simulation is shown in figure 13. There are two main points to make regarding the differences in the results. The first is that XMHD compresses the axial field to a value around 1000 T and is smoothly distributed over the dense part of the liner, whereas for MHD the maximum field strength is somewhat lower, around 800 T and is more nonuniform in its distribution over the liner. The second point is that the liner compression is significantly less than the XMHD case.

The reduced compression for MHD can be seen more clearly at 119 ns in figure 14.

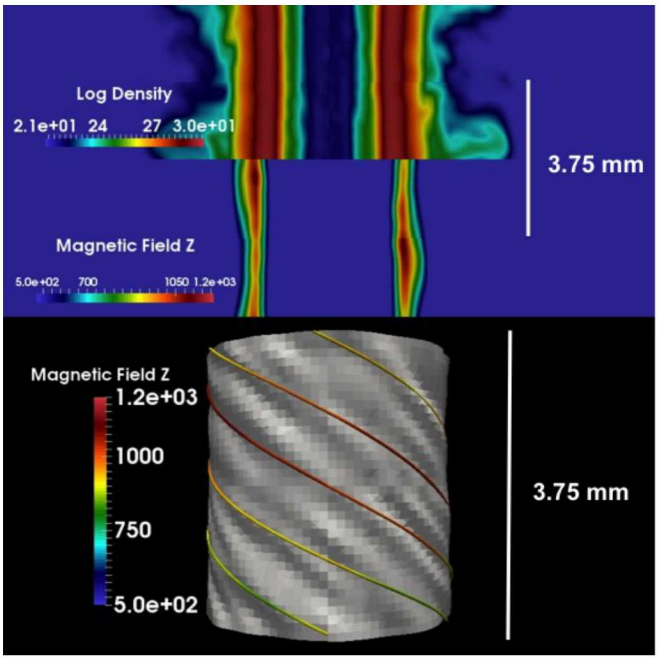

Figure 11. Three-dimensional XMHD simulation of compression of surrounding low-density plasma onto the liner at 100 ns. The displays are top to bottom: the log density in m^{-3}, the axial field in T and a density isosurface at 1.6×10^{28} m^{-3}, which is somewhat above solid Be density. The helical structure is due to the MRT instability.

Note that the iso-density surface value is half that in figure 12 and the axial magnetic field scales are much smaller than in figure 12, showing a much reduced compression of the field inside the liner for MHD. The diameter of the liner is about twice for MHD as for XMHD at this time. The discrepancies in liner compression and axial field magnitude between the XMHD and MHD 3D-simulations are substantial and could easily represent the difference between a good result and a poor result. In this case it would seem that the XMHD result is better insofar as desirability of the final implosion state is concerned.

In order to understand this important difference between MHD and XMHD we have done the following: We used the 3D code that generated the figures but restricted the system to 2D by taking only 2 cells and a correspondingly smaller extent in the periodic axial direction. The result is that the liner compression dynamics in MHD and XMHD are very close as are the magnetic field magnitudes. This verifies that the different results are due to the three-dimensionality. We find that MHD in 3D tends to have considerably more trailing mass in the plasma compression stage than XMHD. This trailing mass sup-

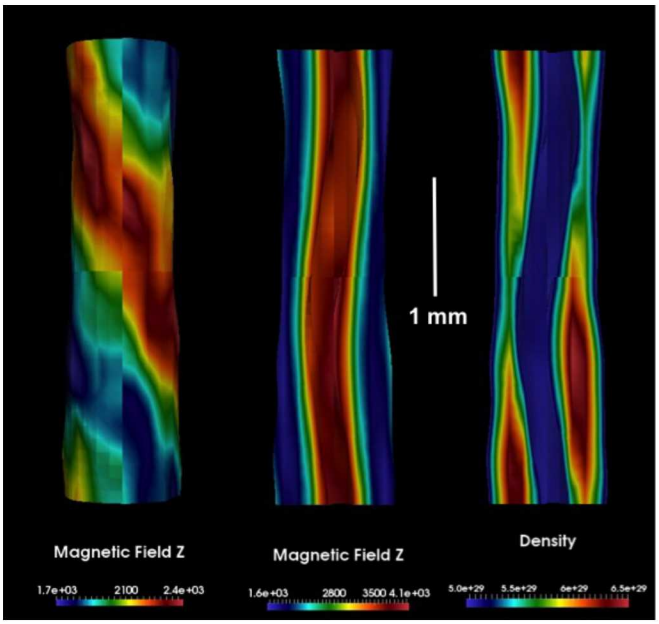

Figure 12. Plots showing the external and internal iso-density surfaces at $4 \times 10^{29}\mathrm{m}^{-3}$ for the 3D XMHD simulation in figure 11 at 119 ns. The color scale for the left and center panels is the axial field strength in T and the right panel is the density in m^{-3}. The middle and right panels display the surfaces cut at the $x = 0$ plane, which is not an isosurface. The cut cross-section shows the density variation inside the isosurfaces

ports halo currents that reduce the current at the liner by a fair amount (roughly 15-20%) thereby reducing the $\mathbf{J} \times \mathbf{B}$ force on the dense liner by an amount sufficient to explain the difference in the implosion time. XMHD does not have either significant halo current or trailing mass and the azimuthal field closely follows a $1/r$ falloff beginning at 1, or at most, 2 mm from the liner. MHD on the other hand begins a $1/r$ falloff about 5 mm from the liner surface where it agrees with the XMHD magnetic field profile, as it should due to the boundary conditions. The reason why MHD produces more trailing mass than XMHD remains unsolved and will require further work that we reserve for a future paper.

To demonstrate the effect of a vacuum resistivity we show in figure 13 the result for an MHD simulation using the same setup as figure 11 but with the resistivity having an additional term that becomes large when the density approaches the density floor. Note that the axial magnetic field is much weaker than figure 11 and the MRT perturbations

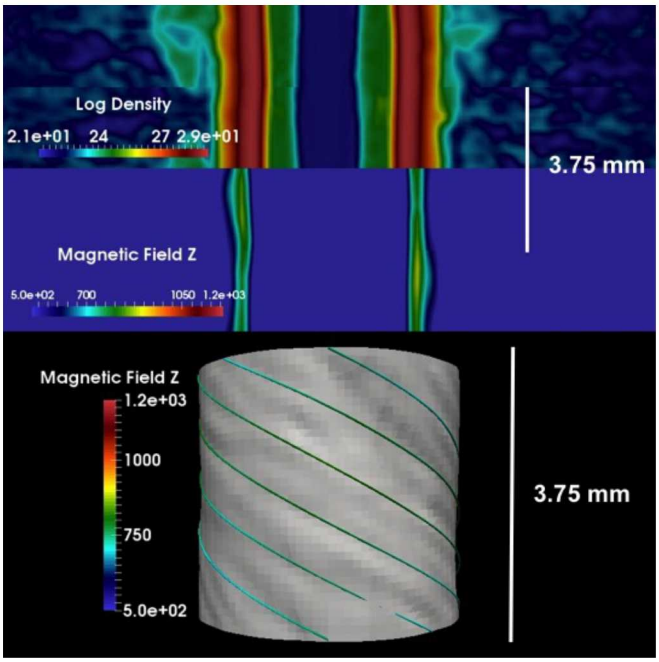

Figure 13. Three-dimensional MHD simulation of compression of surrounding low-density plasma onto the liner at 100 ns to compare with the XMHD simulation in figure 11. The displays are top to bottom the log density in m^{-3}, the axial field in T and a density isosurface at 1.6×10^{29} m^{-3}, which is somewhat above solid Be density. Note that the helical structure is less pronounced than in the XMHD case shown in figure 11.

are essentially axisymmetric. This result cautions against the use of a vacuum resistivity, if it can be avoided, in attempting to capture the helical MRT by the flux compression process.

C. Three-dimensional simulation with ablation from the feed

The final result we show is a 3D simulation of the feed and liner geometry using the same dimensions shown in figure 1, except that the geometry is now fully three dimensional. The plasma is allowed to ablate from all surfaces and the ablation is controlled by selecting the buffer parameter discussed in Sec. III D to a value of 1.01. In figure 14 is shown the iso-density surface at 10^{28} m^{-3} of the liner section. A helical MRT perturbation is clearly evident on the surface and the perturbations match the pitch of the field lines shown. The wavelength of the perturbations are close to the experimentally observed

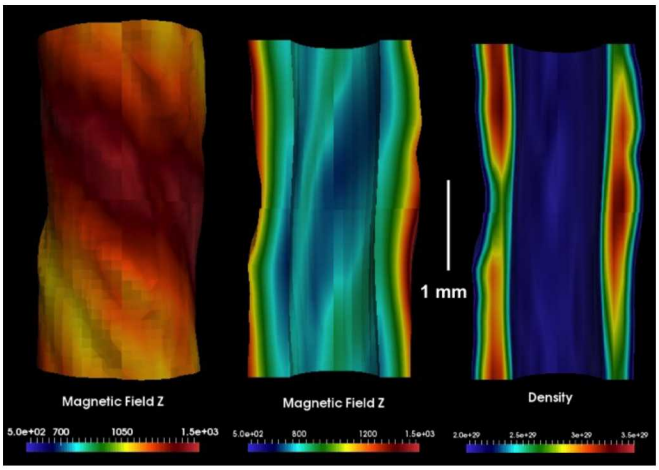

Figure 14. Plots showing the external and internal iso-density surfaces at $2 \times 10^{29} \mathrm{m}^{-3}$ for the 3D MHD simulation in figure 13 at 119 ns. The color scale for the left and center panels is the axial field strength in T and the right panel is the density in m^{-3}. The middle and right panels display the surfaces cut at the $x = 0$ plane, which is not an isosurface. The cut cross-section shows the density variation inside the isosurfaces

.

structures in the MagLIF radiographs.

We do not show the corresponding MHD simulation due to the complications of the differing ablation and magnetic insulation properties of the two models affecting the flux of plasma out of the feed. In keeping the same ablation (buffer) parameter for both the XMHD and MHD cases, which was set to 1.01, the MHD ablation rate is such that MHD simulations exhibit considerable shorting of the current in the feed gap leading to a significant delay in the current delivered to the liner; hence there is a delayed implosion of several 10's of nanoseconds. For this reason we do not show MHD results as such a comparison would be misleading. At the present time we have not had the opportunity to perform a full geometry high-resolution and expensive simulation using the improvements made to the 3D code that allow a fair comparison of XMHD and MHD. The simulations presented in figures 11 - 15 do however have these improvements and we believe are sufficient for the goals of this paper.

It has been well established from numerous MHD simulations that the character of the MagLIF MRT is close to m=0 (sausage-like) unless helical perturbations are preimposed.[3]

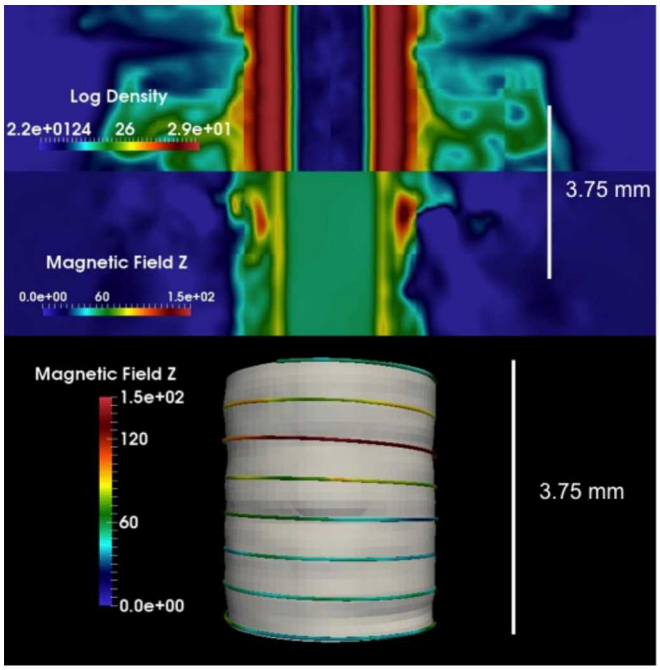

Figure 15. Three-dimensional MHD simulation of compression of surrounding low-density plasma onto the liner in which a vacuum resistivity model is used to suppress low-density currents. The displays are top to bottom: the log density in m^{-3}, the axial field in T and a density isosurface at 10^{28} m^{-3}. Note the absence of the helical MRT instability and the low value of the axial field.

That is, MHD as it was applied to the experiment did not lead to strong axial field enhancement near the surface of the liner. We have presented results that may help explain the reasons previous simulations did not find the helical structuring.

V. DISCUSSION AND CONCLUSIONS

The simulations presented in this paper lend strong support that the helical instability observed in MagLIF is an MRT instability resulting from the compression of the applied axial field onto the surface of the liner by low-density plasma ablated into the region surrounding the liner. Our results suggest that previous MHD simulations that have not found the helical structuring without imposing initial helical perturbations may not have found this mechanism either because the low-density plasma was not generated or because it was treated in a manner that dissipates magnetic flux. We have shown that

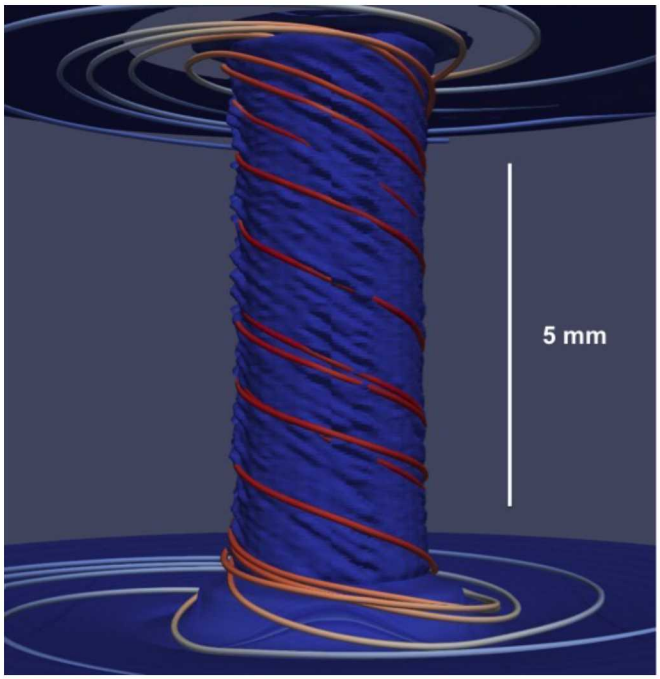

Figure 16. Iso-density surface at $3 \times 10^{28} \mathrm{m}^{-3}$ for a 3D XMHD simulation at 110 ns that includes the feed section that is allowed to ablate. This plot only shows the liner section. The feed section has the same dimensions as in figure 1.

using a floor density that is too high can strongly inhibit ablation from surfaces. For MHD simulations in which low-density plasma is initialized or ablated from metal surfaces, the treatment of the low-density plasma using a vacuum resistivity can dissipate the axial flux to the extent that the axial field on the liner would be much less than the azimuthal field. In either case, for no ablation plasma or with the use of a vacuum resistivity, we do not expect strong compression of the axial field onto the liner.

With respect to producing the helical instability, we have managed to produce comparable results using XMHD and MHD models. Thus we conclude that the failure to produce the helical instability in previous MHD simulations is not a fundamental failing of MHD. The reasons for not generating a helical instability are probably two-fold. The manner in which MHD treats low-density plasma introduces complications that make it difficult to achieve similar results to XMHD, which is more forgiving in not having thermal runaway issues at low-densities. At least this was the case for our numerical algorithm. The other, perhaps more likely reason, is that too high of a density floor was

used in previous simulations. A high-density floor does not allow for an initialization of sufficiently low-density plasma such as to prevent an implosion delay and greatly inhibits plasma emission or ablation from surfaces. We have found that low-density plasma in the range of, or less than, 10^{23} m^{-3} is required to produce reasonable results for either model. We cannot say for sure how other codes may have failed to produce the results we have presented, but hopefully our results will help others understand the reasons. Also, very importantly, if low-density plasma must be included to account for current losses or flux compression, then the Hall term is necessary if the dynamics is to be computed accurately.

An important and challenging effort in computational plasma physics, especially in the national laboratories, is the development of models and algorithms that have a good degree of predictive capability. In this regard, for fluid modeling the results presented in this paper are clear to us, that accounting for the dynamics of plasma at a density that is often neglected in MHD modeling is essential for predictability and that inclusion of the Hall term in the generalized Ohm's law is necessary if the low-density dynamics are to be computed correctly.

The results presented here are not specific to the MagLIF concept. In general, the Hall effect is expected to be important whenever the ion inertial length is comparable to the scale of the plasma. Effects related to the axial field compression and amplification process discussed here should apply to other HED plasma experiments such as gas puff Z-pinches (GPZ) with an applied axial field[18].

ACKNOWLEDGEMENTS

The work of CES and NDH was funded by the National Nuclear Security Administration stewardship sciences academic program under Department of Energy cooperative agreement DE-NA0001836 and Department of Energy Grant DE-FOA-0003764. The work of MRM was funded by Sandia National Laboratories. Sandia National Laboratories is a multimission laboratory managed and operated by National Technology and Engineering Solutions of Sandia LLC, a wholly owned subsidiary of Honeywell International Inc. for the U.S. Department of Energys National Nuclear Security Administration under contract DE-NA0003525. The authors would also like to acknowledge stimulating

and helpful discussions with Prof. David Hammer, Dr. Alexander Velikovich, Prof. Ryan McBride, Dr. Patrick Knapp, Dr. John Greenly, Dr. Thomas Gardiner and Dr. James Hammer.

REFERENCES

[1]S. A. Slutz and R. A. Vesey, Phys. Rev. Lett. 108, 025003 (2012).

[2]Schmit, P. F. and Knapp, P. F. and Hansen, S. B. and Gomez, M. R. and Hahn, K. D. and Sinars, D. B. and Peterson, K. J. and Slutz, S. A. and Sefkow, A. B. and Awe, T. J. and Harding, E. and Jennings, C. A. and Chandler, G. A. and Cooper, G. W. and Cuneo, M. E. and Geissel, M. and Harvey-Thompson, A. J. and Herrmann, M. C. and Hess, M. H. and Johns, O. and Lamppa, D. C. and Martin, M. R. and McBride, R. D. and Porter, J. L. and Robertson, G. K. and Rochau, G. A. and Rovang, D. C. and Ruiz, C. L. and Savage, M. E. and Smith, I. C. and Stygar, W. A. and Vesey, R. A., Phys. Rev. Lett., 113, 155004 (2014)

[3]T. J. Awe, C. A. Jennings, R. D. McBride, M. E. Cuneo, D. C. Lamppa, M. R. Martin, D. C. Rovang, D. B. Sinars, S. A. Slutz, A. C. Owen, K. Tomlinson, M. R. Gomez, S. B. Hansen, M. C. Herrmann, M. C. Jones, J. L. McKenney, G. K. Robertson, G. A. Rochau, M. E. Savage, D. G. Schroen, and W. A. Stygar, Phys. Plasmas 21, 056303 (2014)

[4]T. J. Awe, R. D. McBride, C. A. Jennings, D. C. Lamppa, M. R. Martin, D. C. Rovang, S. A. Slutz, M. E. Cuneo, A. C. Owen, D. B. Sinars, K. Tomlinson, M. R. Gomez, S. B. Hansen, M. C. Herrmann, J. L. McKenney, C. Nakhleh, G. K. Robertson, G. A. Rochau, M. E. Savage, D. G. Schroen, and W. A. Stygar, Phys. Rev. Lett. 111, 235005 (2013)

[5]D. A. Yager-Elorriaga, P. Zhang, A. M. Steiner, N. M. Jordan, Y. Y. Lau, and R. M. Gilgenbach, Phys. Plasmas 23, 101205 (2016)

[6]P. F. Knapp, M. R. Martin, D. H. Dolan, K. Cochrane, D. Dalton, J.-P. Davis, C. A. Jennings, G. P. Loisel, D. H. Romero, I. C. Smith, E. P. Yu, M. R. Weis, T. R. Mattsson, R. D. McBride, K. Peterson, J. Schwarz, and D. B. Sinars, Phys. Plasmas 24, 042708 ; https://doi.org/10.1063/1.4981206 (2017)

[7]C. A. Jennings, M. E. Cuneo, E. M. Waisman, D. B. Sinars, D. J. Ampleford, G. R. Bennett, W. A. Stygar, and J. P. Chittenden, Phys. Plasmas 17, 092703 (2010)

[8]Ryutov, D. D., Awe, T. J., Hansen, S. B., McBride, R. D., Peterson, K. J., Sinars, D. B., and Slutz, S. A. (2014). Effect of axial magnetic flux compression on the magnetic Rayleigh-Taylor instability (theory). In AIP Conference Proceedings (Vol. 1639, pp. 63-66). [4904778] American Institute of Physics Inc.. DOI: 10.1063/1.4904778

[9]C.E. Seyler and M. R. Martin, Phys. Plasmas 18, 012703 (2011)

[10]X. Zhao. Y. Yang, and C. E. Seyler, J. Comp. Phys., 278, 400-415 (2014)

[11]R. A. McBride and S. A. Slutz, Phys. Plasmas 22, 052708 (2015)

[12]E. F. Toro, M. Spruce, and W. Speares, Restoration of the contact surface in the Harten-Lax-van Leer Riemann solver. Shock Waves. Vol. 4, pages 25-34, (1994)

[13]P. Batten, N. Clark, C. Lambert, and D. M. Causon, SIAM J. Sci. Comput. 18, No. 6, (1997)

[14]T. I. Gombosi, G. Toth, D. L. De Zeeuw, K. C. Hansen, K. Kabin, and K. G. Powell, J. Comp. Phys., 177, DOI: 10.1006/jcph.2002.7009, (2002)

[15]S. B. Tannenbaum, Plasma Physics, pp. 65, McGraw-Hill, (1967)

[16]A. S. Kingsep, Yu. V. Mohkov, and K. V. Chukbar, Sov. J. Plasma Phys. 10, 495, (1984)

[17]M. R. Gomez, S. A. Slutz, A. B. Sefkow, D. B. Sinars, K. D. Hahn, S. B. Hansen, E. C. Harding, P. F. Knapp, P. F. Schmit, C. A. Jennings, T. J. Awe, M. Geissel, D. C. Rovang, G. A. Chandler, G. W. Cooper, M. E. Cuneo, A. J. Harvey-Thompson, M. C. Herrmann, M. H. Hess, O. Johns, D. C. Lamppa, M. R. Martin, R. D. McBride, K. J. Peterson, J. L. Porter, G. K. Robertson, G. A. Rochau, C. L. Ruiz, M. E. Savage, I. C. Smith, W. A. Stygar, and R. A. Vesey, Phys. Rev. Lett., 113, 155003 (2014)

[18]A. L. Velikovich, Naval Research Laboratory (personal communication, 2017)